ADVANCED MATERIALS TECHNOLOGIES
www.advmattechnol.de

Measuring and Simulating the Transient Packing Density During Ultrasound Directed Self-Assembly and Vat Polymerization Manufacturing of Engineered Materials

*Soheyl Noparast, Fernando Guevara Vasquez, Mathieu Francoeur, and Bart Raeymaekers**

Ultrasound-directed self-assembly (DSA) uses ultrasound waves to organize and orient particles dispersed in a fluid medium into specific patterns. Combining ultrasound DSA with vat photopolymerization (VP) enables manufacturing materials layer-by-layer, wherein each layer the organization and orientation of particles in the photopolymer is controlled, which enables tailoring the properties of the resulting composite materials. However, the particle packing density changes with time and location as particles organize into specific patterns. Hence, relating the ultrasound DSA process parameters to the transient local particle packing density is important to tailor the properties of the composite material, and to determine the maximum speed of the layer-by-layer VP process. This paper theoretically derives and experimentally validates a 3D ultrasound DSA model and evaluates the local particle packing density at locations where particles assemble as a function of time and ultrasound DSA process parameters. The particle packing density increases with increasing particle volume fraction, decreasing particle size, and decreasing fluid medium viscosity is determined. Increasing the particle size and decreasing the fluid medium viscosity decreases the time to reach steady-state. This work contributes to using ultrasound DSA and VP as a materials manufacturing process.

1. Introduction

Ultrasound-directed self-assembly (DSA) uses the acoustic radiation force associated with a standing ultrasound wave field to organize and orient spherical[1] or high aspect ratio particles[2] dispersed in a fluid medium into specific patterns. It finds application in a broad spectrum of engineering applications, such as noncontact manipulation of particles and objects for precise handling or quality control,[3–5] levitated displays,[6–8] and organizing[9–11] and separating particles and cells, e.g., in lab-on-a-chip devices.[12–14]

Ultrasound DSA is also useful to manufacture engineered composite materials with tailored properties. For instance, it integrates with formative manufacturing processes such as mold casting[15–17] and freeze casting,[18,19] and it integrates with additive manufacturing (AM) processes, such as direct ink writing (DIW)[20–22] and vat photopolymerization (VP).[23–27] Specifically, AM enables the manufacturing of free-form engineered polymer matrix composite materials in a layer-by-layer fashion, wherein each layer ultrasound DSA provides the ability to organize and orient the filler (particles) in a specific pattern to tailor the properties of the composite material.[23]

The forces that act on a spherical particle in an ultrasound wave field have been studied in both inviscid[28,29] and viscous[30] fluid media. Theoretical studies of the acoustic radiation force began with King,[31] and Yosioka and Kawasima,[32] who considered incompressible and compressible spherical particles dispersed in an inviscid fluid medium, respectively. However, it was Gor'kov[28] who presented a generalized acoustic radiation force theory for compressible spherical particles smaller than the acoustic wavelength, dispersed in an inviscid fluid

S. Noparast, B. Raeymaekers
Department of Mechanical Engineering
Virginia Tech
Blacksburg, VA 24061, USA
E-mail: bart.raeymaekers@vt.edu

The ORCID identification number(s) for the author(s) of this article can be found under https://doi.org/10.1002/admt.202301950

DOI: 10.1002/admt.202301950

F. Guevara Vasquez
Department of Mathematics
University of Utah
Salt Lake City, UT 84112, USA

M. Francoeur
Department of Mechanical Engineering
McGill University
Montréal, Québec H3A 0C3, Canada

M. Francoeur
Department of Mechanical Engineering
University of Utah
Salt Lake City, UT 84112, USA

medium. The acoustic radiation force derives from scattering, which results from the acoustic contrast between the particles and the fluid medium, and it drives the particles to the locations where the acoustic radiation potential is locally minimum and the acoustic radiation force approaches zero.[28] These locations coincide with nodes and antinodes of the standing ultrasound wave, depending on the density and compressibility of the particles and the fluid medium.[33]

More recently, Settnes and Bruus[30] expanded Gor'kov's theory to account for fluid medium viscosity, and they demonstrated that the acoustic radiation force changes by multiple orders of magnitude in a viscous compared to an inviscid fluid medium. Additionally, a secondary radiation force or acoustic interaction force results from scattering between particles in close proximity. König[34] and Bjerknes[35] theoretically studied the acoustic interaction force between incompressible and compressible spheres, respectively, followed by other researchers who considered incompressible particles in an inviscid[36–38] and viscous[39] fluid medium, and compressible particles in an inviscid fluid medium.[40]

Based on a fundamental understanding of the forces acting on particles in an ultrasound wave field, researchers have solved both the forward[28,29,41] and inverse[1,42,43] ultrasound DSA problems that relate the organization and orientation of the particles in the fluid medium to the operating parameters (amplitude, phase, frequency) of any number and spatial arrangement of ultrasound transducers. The literature documents results for ultrasound DSA of spherical particles in 2D[1,44,45] and 3D,[43,46] and high-aspect-ratio particles in 2D[2] and 3D.[4,47,48]

During ultrasound DSA, the concentration of particles in the fluid medium changes as a function of time and location[49] and, specifically, the local particle packing density increases with time at the locations where particles assemble, as particles agglomerate there. Our group has previously quantified the effect of particle volume fraction, particle size, and fluid medium viscosity on the locations where particles assemble[50] and the steady-state local particle packing density.[51]

However, the transient phenomena that govern the time-dependent motion of particles from their initial dispersed state to their final organized steady-state locations are currently not well understood. Yet, this knowledge is important to advance engineering applications that rely on ultrasound DSA for the manipulation of particles, such as levitated displays and manipulation of cells or particles in biomedical devices. Furthermore, in the context of manufacturing engineered composite materials with ultrasound DSA and VP, it is paramount to understand the transient phenomena during the ultrasound DSA process, because the layer-by-layer VP process requires that particles reach their steady-state locations before a new layer can be cured.

Few researchers have investigated transient phenomena in ultrasound DSA. Specifically, theoretical and experimental studies document the movement of a single spherical particle in a fluid medium during ultrasound DSA in 1D,[52,53] 2D,[54–56] and 3D.[57] These studies demonstrate that ultrasound frequency, longitudinal wave propagation velocity, particle radius, and fluid medium viscosity significantly affect the transient motion of a single spherical particle during ultrasound DSA. In addition, Scholz et al.[55] experimentally studied the transient motion of multiple glass particles dispersed in water during ultrasound DSA, and reported different transient phenomena for ultrasound DSA of multiple spherical particles.

Importantly, no experimentally validated theoretical model exists that describes the transient phenomena of spherical particles dispersed in a viscous fluid medium during ultrasound DSA. However, quantifying the transient local particle packing density as a function of material properties and ultrasound DSA process parameters is essential in the context of using ultrasound DSA in, e.g., manufacturing of engineered composite materials with ultrasound DSA and VP, among other applications. Hence, we theoretically derive and experimentally validate a 3D ultrasound DSA model to simulate the trajectories and interactions of spherical particles dispersed in a viscous fluid medium, as they organize into their steady-state locations. Using this 3D model, we simulate the transient local particle packing density and packing rate at locations where particles assemble as a function of the ultrasound DSA process parameters.

2. Theoretical and Experimental Section

2.1. Theoretical Model

Figure 1 illustrates the theoretical model we implement to simulate the trajectory of many spherical particles dispersed in a viscous fluid medium during ultrasound DSA, as a function of time t, particle volume fraction Φ, particle size a, and fluid medium viscosity η_m. Figure 1a schematically shows a reservoir that contains a mixture of a viscous fluid medium and spherical particles. Two ultrasound transducers attached to opposing walls of the reservoir (orange walls in Figure 1a) establish a standing ultrasound wave field. We simulate the time-averaged acoustic radiation potential U inside the solution domain (see contour lines in color ranging from blue (minima) to yellow (maxima)) using the boundary element method (BEM) based on the Helmholtz equation $\nabla^2\varphi_{\text{inc}} + \tilde{k}^2\varphi_{\text{inc}} = 0$ and Green's third identity. These equations relate the incident ultrasound velocity potential φ_{inc} within the simply closed boundary of the solution domain to the impedance boundary condition, which considers the absorption and reflection of the ultrasound wave field at the boundary of the solution domain. $\tilde{k}$ is the complex wave number that accounts for acoustic attenuation in the viscous fluid medium.[51]

Figure 1b shows the forces that act on a spherical particle with radius a in a viscous fluid medium within a standing ultrasound wave field, superimposed on the time-averaged acoustic radiation potential U (see contour lines with the same color scale as in Figure 1a). We also identify a node and antinode of the standing ultrasound wave field, separated by a half wavelength λ, and we exaggerate the particle size relative to the wavelength for clarity; in reality, $a << \lambda$. A spherical particle experiences the acoustic radiation force $\mathbf{F}_a$, which drives the particle to the locations where the time-averaged acoustic radiation potential U is locally minimum and the acoustic radiation force $\mathbf{F}_a = 0$. Additionally, it is subject to a drag force $\mathbf{F}_d$, which orients in the opposite direction of the particle motion, a gravitational force $\mathbf{F}_g$, and buoyancy force $\mathbf{F}_b$, since the particle is immersed in a viscous fluid medium. We use a repulsive Lennard-Jones-like potential as an interaction force $\mathbf{F}_{LJ}$ to model particle–particle and particle–wall interactions within the simulation domain, which is a subset of the solution domain in the far field of the ultrasound transducers.

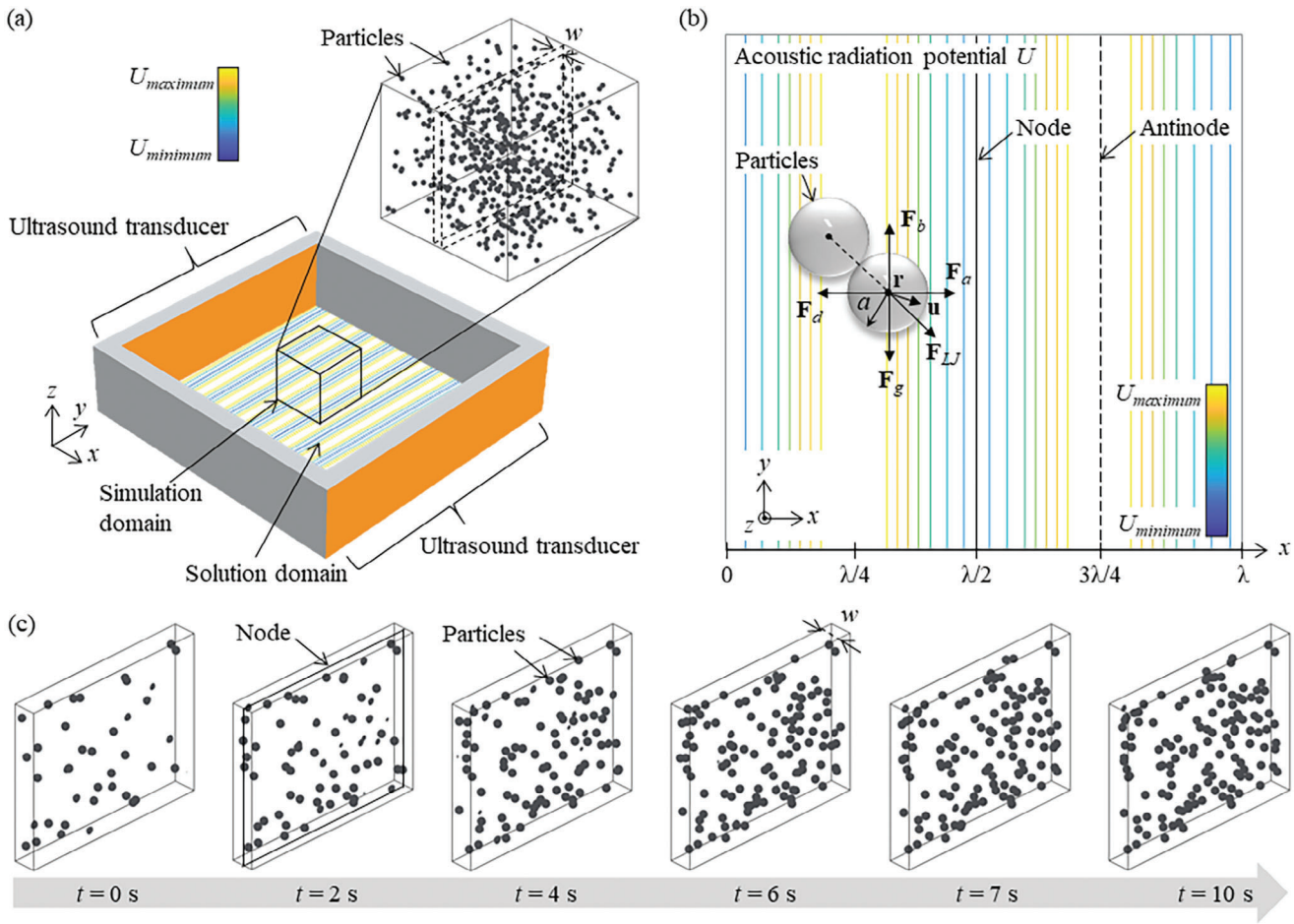

Figure 1. a) Schematic of the 3D ultrasound DSA model, showing a reservoir that contains a mixture of a viscous fluid medium and spherical particles, and with two ultrasound transducers (orange) that establish a standing ultrasound wave field (time-averaged acoustic radiation potential U in color). The reservoir encloses the solution domain, but we only simulate the trajectories of the particles within the simulation domain, which is a subset of the solution domain in the far field of the ultrasound transducers. b) Forces that act on a spherical particle in a viscous fluid medium and in a standing ultrasound wave field (time-averaged acoustic radiation potential U in color). The size of the particles is exaggerated for clarity, in reality, the particle size a << wavelength λ. c) Simulated particle assemble in a domain of width w around a node of standing ultrasound wave field as a function of time t during ultrasound DSA.

We define $N \approx 700$ randomly dispersed, nonoverlapping particles inside the simulation domain in the center of the solution domain (see Figure 1a), and we uniformly scale the size of the simulation domain to achieve a specific particle volume fraction Φ. The velocity potential φ is the sum of the incident velocity potential φ_{inc}, which we calculate using the BEM, and the velocity potential that results from single scattering from all other particles in the simulation domain φ_{sc}. Thus, the velocity potential φ at the location of the i^{th} particle $\mathbf{r}_i$ is[51]

$$\varphi(\mathbf{r}_i) = \varphi_{\mathrm{inc}}(\mathbf{r}_i) + \sum_{\substack{j=1 \\ j \neq i}}^{N} \varphi_{\mathrm{sc}}(\mathbf{r}_i|\mathbf{r}_j) \tag{1}$$

where $\varphi_{\mathrm{sc}}(\mathbf{r}_i|\mathbf{r}_j)$ is the single monopole and dipole scattering velocity potential of the j^{th} particle at location $\mathbf{r}_j$, measured at the location of i^{th} particle $\mathbf{r}_i$. $\varphi_{sc}(\mathbf{r}_i|\mathbf{r}_j)$ accounts for both monopole and dipole scattering, which depend on the compressibility and density contrast between the particles and the fluid medium, respectively. Dipole scattering also depends on the fluid medium viscosity η_{m}, and it considers the thickness of the viscous boundary layer around a particle $\delta = (2\eta_{\mathrm{m}}/\omega\rho_{\mathrm{m}})^{1/2}$, where $\omega = 2\pi f$ and f are the angular and temporal ultrasound wave frequencies, respectively, and ρ_{m} is the density of the fluid medium. We refer to Noparast et al.[51] for a detailed derivation of $\varphi_{sc}(\mathbf{r}_i|\mathbf{r}_j)$.

The ultrasound wave velocity $\boldsymbol{v} = \nabla\varphi$ is the gradient of the ultrasound velocity potential φ. The ultrasound wave pressure $p = i\rho_m\omega\varphi$, with $i = (-1)^{1/2}$. The time-averaged acoustic radiation potential U in a viscous fluid medium is given as[30]

$$U = \frac{4\pi}{3}a^3\left(f_1\frac{\beta_{\mathrm{m}}}{2}\langle p^2\rangle - f_2\frac{3\rho_{\mathrm{m}}}{4}\langle v^2\rangle\right) \tag{2}$$

where $f_1 = 1\text{-}\beta_{\mathrm{p}}/\beta_{\mathrm{m}}$ and $f_2 = \Re\{[2(1\text{-}\gamma)(\rho_p/\rho_{\mathrm{m}}\text{-}1)]/[2\rho_p/\rho_{\mathrm{m}}\text{+}1\text{-}3\gamma]\}$, with $\gamma = -3/2[1+i(1+\delta/a)]\delta/a$. The compressibility of the

spherical particle $\beta_p = 1/[\rho_p(c_{p,c}{}^2\text{-}4c_{p,s}{}^2/3)]$, and the compressibility of the fluid medium $\beta_m = 1/(\rho_m c_m{}^2)$, with ρ_p the density of the particle, and $c_{p,c}$ and $c_{p,s}$ the propagation velocity of the longitudinal and shear wave in the particle.[29] Operators $\langle\bullet\rangle$ and $\Re\{\bullet\}$ calculate the time average over one ultrasound wave period and the real part of an expression, respectively. The acoustic radiation force $\mathbf{F}_a = -\nabla U$ is the negative gradient of the time-averaged acoustic radiation potential U.

The drag force $\mathbf{F}_d$ on each particle inside the simulation domain orients in the opposite direction of the particle velocity $\mathbf{u}$ (see Figure 1b), with $||\mathbf{F}_d|| = 12\pi a^2 \rho_m ||\mathbf{u}||^2 (1 + 3/16Re)/Re$ using Stokes drag force with Oseen's correction. The Reynolds number $Re = 2a\rho_m||\mathbf{u}||/\eta_m$.[58]

The interaction force $\mathbf{F}_{LJ} = -\nabla V_{LJ}$ between pairs of particles[59] derives from a repulsive Lennard–Jones-like potential $V_{LJ} = 4\epsilon_{LJ}(2a/r)^{12}$ and accounts for particle–particle and particle–wall interactions within the simulation domain. We iteratively tune ϵ_{LJ} to prevent particles from occupying the same space when organized in specific locations, by ensuring that the average distance between two contacting particles is $2a$ (+/−2%), or a (+/−2%) for contact between a particle and a wall. We describe the iterative tuning procedure of ϵ_{LJ} in the Appendix, but note that for the range of particle volume fractions used in this work, ϵ_{LJ} has limited influence on the results of the transient ultrasound DSA model.

The simulation of the ultrasound DSA process works as follows. First, we calculate the incident velocity potential φ_{inc} within the solution domain using the BEM based on the Helmholtz equation with complex wave number $\tilde{k}$ to account for the attenuation of the ultrasound wave in a viscous fluid medium. Second, we calculate the velocity potential φ at the location of each particle as the superposition of the incident velocity potential φ_{inc} and scattering velocity potential φ_{sc} of all other particles in the simulation domain (Equation 1). Then, we calculate the time-averaged acoustic radiation potential U, and the corresponding acoustic radiation force $\mathbf{F}_a$ that acts on each particle in the simulation domain.

We calculate the trajectory of each spherical particle inside the simulation domain during the transient ultrasound DSA process as a function of time $0 \le t \le T$, with time step $\Delta t = T/3000$. We use a variable time step $\Delta t = T/3000$ to keep the average distance that particles travel in a single time step sufficiently short to avoid that particles overlap and occupy the same space. At $t = 0$, particles are stationary $||\mathbf{u}|| = 0$, and at $t = T$, particles have reached their steady-state locations at the nodes of the standing ultrasound wave. However, when $t > 0$ they accelerate as a result of the forces acting on them, and they displace toward the closest local minimum of the time-averaged acoustic radiation potential U (blue contour lines in Figure 1a,b). Thus, we determine the location $\mathbf{r}$ and velocity $\mathbf{u}$ of each particle for each time step Δt, accounting for all forces that act on the particle (see Figure 1b) by integrating twice in time the acceleration of each particle.

Furthermore, we calculate the 3D local particle packing density PD_{sim}, for each time step Δt, as the fraction of a cuboid domain of width w around a local minimum of the time-averaged acoustic radiation potential U (where particles assemble) occupied by spherical particles. Figure 1c depicts the domain of width w (black solid box) around a node of the standing ultrasound wave field with particles (gray spheres) that assemble inside the domain, visualized for six different time instances t, starting from $t = 0$ s when particles are randomly dispersed in the simulation domain, until $t = 10$ s when particles and PD_{sim} reach steady-state. We choose the width of the domain w to be proportional to the particle radius a (see Section 2.2) and compare it later in Figure 8 to choosing w constant and independent of a.

We perform a nondimensional parameter study to quantify the 3D local particle packing density PD_{sim} as a function of ultrasound DSA process parameters, including time t, particle volume fraction Φ, particle size a, and fluid medium viscosity η_m. Using the Buckingham π theorem, we determine that at least four nondimensional parameters are required to describe this system (see **Table 1**); i) the nondimensional particle size $0.05 \le K_1 = ka \le 0.20$, which we select to satisfy the Rayleigh regime assumption ($ka << 1$) where $k = \omega/c_m$ is the real wave number, ii) the nondimensional fluid medium viscosity $0.07 \le K_2 = \eta_m/\rho_m \lambda c_m \le 0.27$, which we define to span the viscosity range of commercial photopolymer resins $100 \le \eta_m \le 400$ mPa·s, where $\lambda = c_m/f$, iii) the nondimensional time $0 \le K_3 = ft \le 150$, which captures the entire transient time-span from initial dispersion to steady-state, for all combinations of parameters, and iv) the particle volume fraction $0.5 \le \Phi \le 22.5\%$, which we select to achieve maximum local particle packing density during steady-state. We note that the units of the fluid medium viscosity η_m in K_2 and the temporal ultrasound frequency f in K_3 are mPa·s and MHz, respectively. The parameter study quantifies the transient local particle packing density PD_{sim} as a function of K_1, K_2, K_3, Φ. To characterize the transient local particle packing density PD_{sim}, we define two additional nondimensional parameters: the nondimensional packing time $K_3{}^*$, which is the nondimensional time K_3 when the local particle packing density reaches 90% of its steady-state value, and the nondimensional packing rate $\delta PD_{sim}/\delta K_3$, which is the nondimensional rate at which the transient local particle packing density PD_{sim} changes from 20% to 80% of its steady-state value.

2.2. Experimental Validation

Figure 2 schematically shows the experimental setup, which integrates a 30 mm × 30 mm acrylic reservoir with two ultrasound transducers (PZT-4, center frequency $f_c = 1.5$ MHz, piezoelectric constant $d_{33} = 285 \times 10^{-12}$ m V^{-1},[60] Steminc, FL, USA) in a VP digital light processing (DLP) printer (mUVe 1.1 DLP, Grand Rapids, MI, USA). We use photopolymer resin (3DRS standard V2 gray resin, 3D Resin Solutions, IL, USA) and photopolymer resin diluted with 5 wt% of isopropyl alcohol, in combination with spherical aluminum microparticles ($a = 15$ and 22 µm, US5005 solid aluminum spherical powder, US Research Nanomaterials Inc., TX, USA). **Table 2** summarizes the material properties of the particles and the fluid medium. We determine the longitudinal wave propagation velocity of the fluid medium using a pulse-echo time-of-flight measurement,[61] and the fluid medium viscosity using a rheometer (Discovery HR 30, TA Instruments, New Castle, DE, USA).

We choose the range of particle volume fraction Φ, particle size a, fluid medium viscosity η_m, and time t based on considerations of practical feasibility of the experiments. We select $0.50 \le \Phi \le 1.50\%$ because increasing Φ increases the attenuation of

Table 1. Nondimensional ultrasound DSA process parameters.

Nondimensional parameter	Definition	Range	Notes
Particle size, K_1	$K_1 = ka$	$0.05 \leq K_1 \leq 0.20$	Satisfies the Rayleigh regime assumption ($ka << 1$).
Fluid medium viscosity, K_2	$K_2 = \eta_m/\rho_m \lambda c_m$	$0.07 \leq K_2 \leq 0.27$	Spans the viscosity range of commercial photopolymer resins $100 \leq \eta_m \leq 400$ mPa s.
Time, K_3	$K_3 = ft$	$0 \leq K_3 \leq 150$	Covers the entire time span from initial dispersion to steady-state, for all combinations of parameters.
Particle volume fraction, Φ	Particle volume	$0.5 \leq \Phi \leq 22.5\%$	Achieves maximum local particle packing density during steady-state.

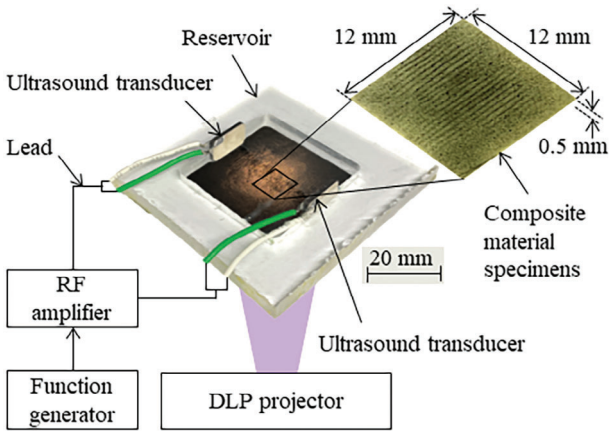

Figure 2. Schematic of the experimental setup, which integrates an acrylic reservoir with two ultrasound transducers in a VP DLP printer. The reservoir contains a mixture of photopolymer and aluminum microparticles, and a function generator and RF amplifier drive the ultrasound transducers to organize the particles into a line pattern that corresponds to the nodes of the standing ultrasound wave field between both ultrasound transducers. Exposure to UV light cures a square single-layer composite material specimen.

the ultrasound wave due to scattering, and it also increases the effective viscosity, which decreases the acoustic radiation force $||\mathbf{F}_a||$ and increases the drag force $||\mathbf{F}_d||$ on the particles. Consequently, it reduces the ability to organize particles in the viscous fluid medium. The curing time of the photopolymer resin also increases with increasing Φ,[62] which could distort the organization of the particles. We choose particle sizes $a = 15$ and 22 µm ($K_1 = 0.10$ and 0.15) to satisfy the Rayleigh regime assumption ($K_1 = ka << 1$). Additionally, the particles are small enough to not precipitate to the floor of the reservoir, yet they are large enough to be observed under an optical microscope. The fluid medium viscosity $\eta_m = 126$ and 218 mPa.s ($K_2 = 0.09$ and 0.15) matches the viscosity of typical commercial photopolymer resins. Finally, we define time $0 \leq t \leq 30$ s ($0 \leq K_3 \leq 45$) to ensure capturing the entire transient behavior of the local particle packing density PD_{exp} during ultrasound DSA, using all combinations of Φ, K_1, and K_2.

We disperse a volume fraction Φ particles in the viscous fluid medium using a magnetic stirrer, and energize the ultrasound transducers with a function generator (Tektronix AFG 3102, Beaverton, OR, USA) and a radio frequency (RF) power amplifier (E&I 2100L, Rochester, NY, USA) to organize the particles into line patterns that correspond to the nodes of the standing ultrasound wave field between both ultrasound transducers. The input peak-to-peak voltage of the ultrasound transducers $V_{p\text{-}p} = 21$ V. This translates to a velocity amplitude of the ultrasound transducer surface $|v| = 2.8 \times 10^{-2}$ m $^{-1}$s, based on the piezoelectric constant of the ultrasound transducers, which we require as a boundary condition in the simulations with the BEM method (see Section 2.1). After ultrasound DSA, we cure a single layer 12 mm × 12 mm composite material specimen with a 12 s exposure time, and a 120 s post-cure time outside the VP setup to eliminate any liquid photopolymer. Figure 2 shows a typical composite material specimen after curing and post-curing ($\Phi = 1.00\%$, $K_1 = 0.10$, $K_2 = 0.09$, and $K_3 = 15$).

To perform a full-factorial study of the local particle packing density PD_{exp} as a function of Φ, K_1, K_2, and K_3, we manufacture 72 composite material specimens (3 (Φ) x 2 (K_1) x 2 (K_2) x 6 (K_3)) using the experimental setup of Figure 2. Additionally, we perform three repeat measurements of each combination of parameters, for a total of 216 composite material specimens.

We experimentally measure the local particle packing density PD_{exp} as the area fraction of a rectangular domain of width w around the location where particles assemble, occupied by the particles. The fraction of an area covered by particles approximates the volumetric particle packing density, as first

Table 2. Material properties of the particles and viscous fluid media.

Material	Density, ρ [kg m^{-3}]	Longitudinal wave propagation velocity, c [m $^{-1}$s]	Shear wave propagation velocity, c [m $^{-1}$s]	Viscosity, η_m [mPa s]
Spherical aluminum microparticles	2710[63]	$c_{c,p} = 6420$[63]	$c_{s,p} = 3040$[63]	–
Standard photopolymer resin	1100	$c_m = 1420$	–	218
Diluted standard photopolymer resin	1079	$c_m = 1409$	–	126

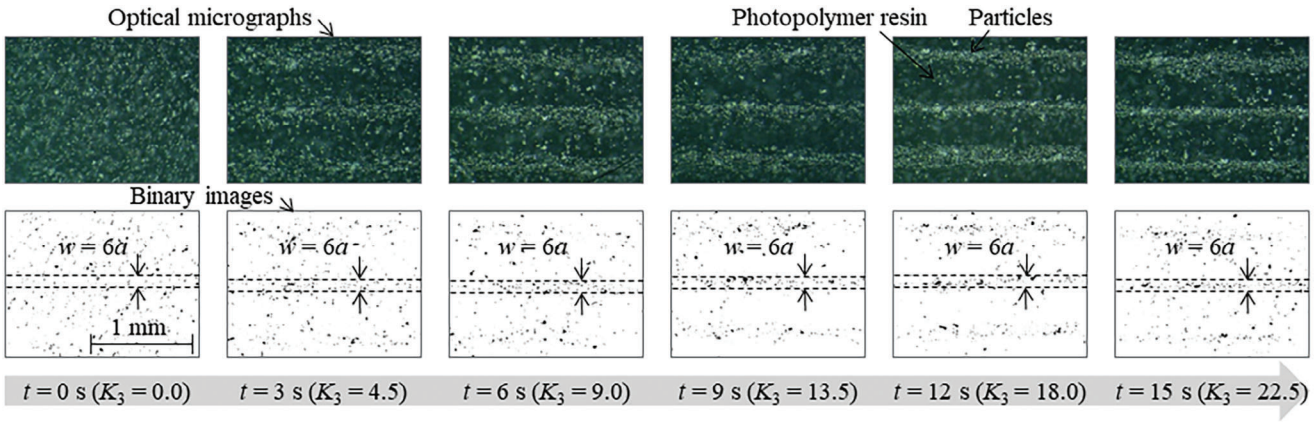

Figure 3. Methodology to measure the local particle packing density PD_{exp}, showing optical micrographs with corresponding binary images as a function of time t for $\Phi = 1.00\%$, $K_1 = 0.10$, and $K_2 = 0.09$, covering domain $w = 6a$.

suggested by Delesse in 1848[64] and later theoretically and experimentally demonstrated by Underwood[65] and Weibel.[64,66] We also verified the accuracy of this approximation using the 3D theoretical model and determined a 4% maximum error for $\Phi = 1.5\%$.

Figure 3 illustrates the measurement methodology, showing optical micrographs (1.5 µm spatial resolution, 180X magnification, AmScope, CA, USA) with the corresponding binary images as a function of time t (K_3) for $\Phi = 1.00\%$, $K_1 = 0.10$, and $K_2 = 0.09$, of locations where we qualitatively detect organization of the spherical aluminum microparticles. We focus the optical microscope on the top surface of the composite material specimen to only capture particles (silver) on the surface (green), and not in the bulk of the specimen. We binarize the optical micrographs using a threshold that equates the particle area fraction of the entire field of view to the particle volume fraction Φ dispersed in the photopolymer. This minimizes the effect of external influences, such as lighting conditions and glare, on the binarization of the image. We measure the particle area fraction as the number of black pixels within a domain $w = Ma$ centered around a location where particles assemble divided by the total number of pixels within the domain (see Figure 3). We select $M = 6$, i.e., $w = 6a$ to enclose most particles that assemble at the node of a standing ultrasound wave field, based on experiments with $\Phi = 1.00\%$, $K_1 = 0.10$, and $K_2 = 0.09$. We repeat each measurement three times for composite material specimens and report the average, minimum, and maximum values of the local particle packing density PD_{exp}.

3. Results and Discussion

3.1. Experimental Validation

Figure 4 shows the simulated PD_{sim} (lines) and experimental PD_{exp} (solid markers) local particle packing density as a function of the nondimensional time K_3, for three particle volume fractions $\Phi = 0.5$, 1.0, 1.5%, and for a) $K_1 = 0.10$ and $K_2 = 0.09$, b) $K_1 = 0.15$ and $K_2 = 0.09$, c) $K_1 = 0.10$ and $K_2 = 0.15$, (d) $K_1 = 0.15$ and $K_2 = 0.15$, i.e., the rows and columns represent constant K_2 and K_1, respectively. The solid markers represent the average of three measurements, and the error bars show the minimum and maximum. Figure 4 illustrates excellent agreement between the theoretical simulations and experimental results, and we determine a maximum $|PD_{exp} - PD_{sim}| = 0.9\%$ error for $\Phi = 1.5\%$, $K_1 = 0.05$, $K_2 = 0.15$, and $K_3 = 22.5$. Additionally, **Figure 5** shows optical micrographs (green = resin, silver = particles) and the corresponding binary images (white = resin, black = particles) of the composite material specimens as a function of nondimensional time K_3 for selected data points of Figure 4.

We observe from Figures 4 and 5 that the local particle packing density at locations where particles assemble increases with increasing nondimensional time K_3 because the number of particles that assemble at a specific location increases. The local particle packing density reaches steady-state when almost all particles have assembled into the specific location, and no additional particles are available to assemble at that location. Furthermore, the local particle packing density increases with increasing particle volume fraction Φ because the number of particles dispersed in the photopolymer resin increases, which the comparison of Figure 5a,b illustrates. Figure 4a–d shows that increasing the nondimensional particle size K_1 decreases the local particle packing density for constant particle volume fraction Φ because the number of particles to obtain a specific Φ decreases with increasing K_1, which is evident from the comparison of Figure 5a,c. Figure 4a–d, shows that increasing the nondimensional fluid medium viscosity K_2 decreases the transient local particle packing density for constant particle volume fraction Φ because increasing the fluid medium viscosity increases the drag force on the particles $||\mathbf{F}_d||$ and decreases their velocity $||\mathbf{u}||$, which delays their assembly at specific locations. However, the steady-state local particle packing density remains unaffected by changing the fluid medium viscosity, because it only depends on the number of particles dispersed in the fluid medium. Figure 5a,d illustrate the effect of increasing the nondimensional fluid medium viscosity K_2.

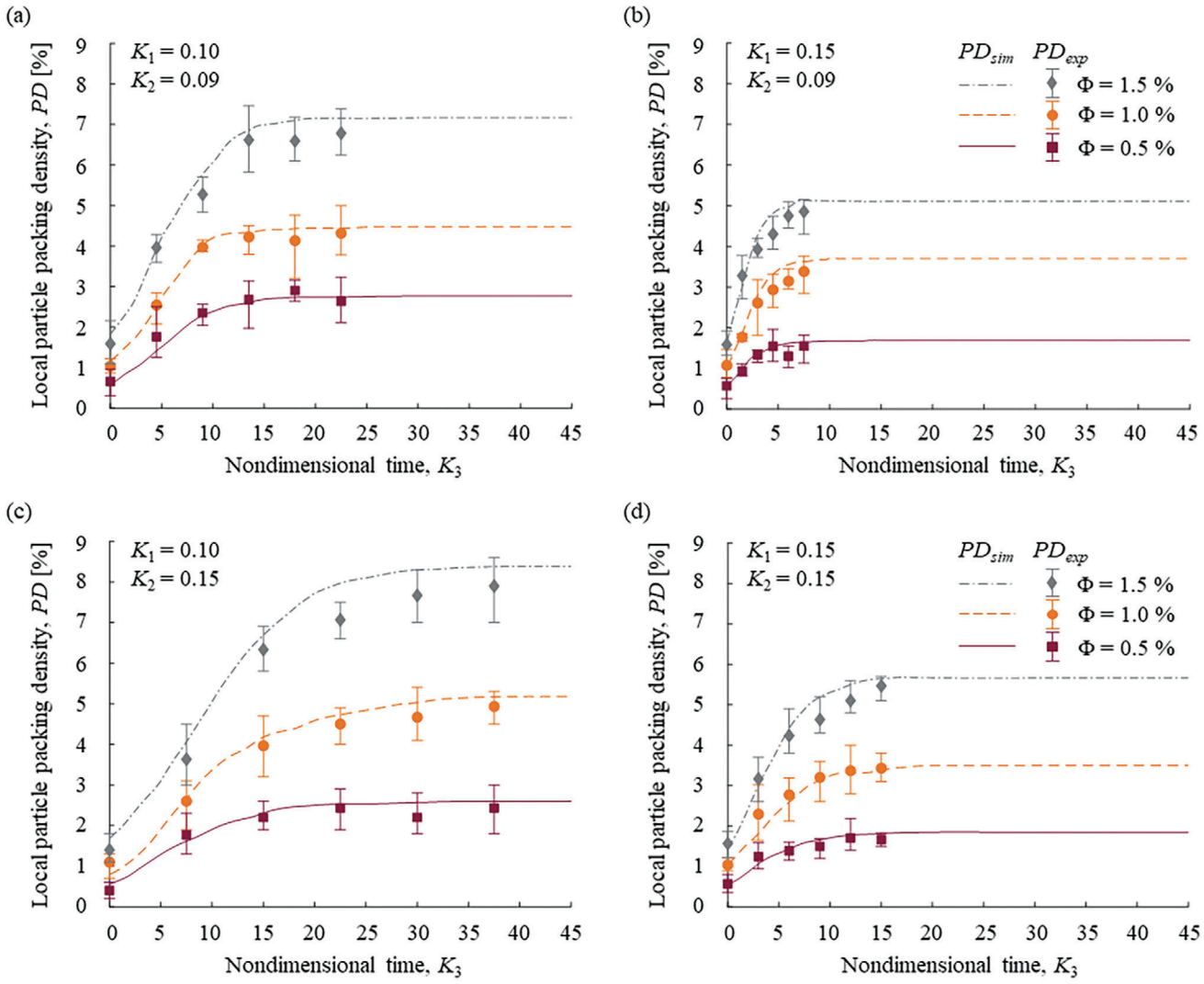

Figure 4. Transient and steady-state local particle packing density within the pattern features that result from ultrasound DSA (node of the standing ultrasound wave field) as a function of nondimensional time K_3, showing simulation PD_{sim} (lines) and experiment PD_{exp} (solid markers) results for particle volume fraction $\Phi = 0.5\%$ (solid maroon line and maroon square), $\Phi = 1.0\%$ (dashed orange line and orange circle), and $\Phi = 1.5\%$ (dash-dot gray line and gray diamond), and for a) $K_1 = 0.10$ and $K_2 = 0.09$ b) $K_1 = 0.15$ and $K_2 = 0.09$, c) $K_1 = 0.10$ and $K_2 = 0.15$, d) $K_1 = 0.15$ and $K_2 = 0.15$.

3.2. Simulation Results and Parameter Study

We also use the 3D theoretical model to illustrate the effect of particle volume fraction Φ, nondimensional particle size K_1, nondimensional fluid medium viscosity K_2, and nondimensional time K_3 on the transient local particle packing density PD_{sim} during ultrasound DSA, covering the entire ultrasound DSA process envelope, i.e., beyond the parameter ranges we have experimentally validated. **Figure 6** shows the transient local particle packing density PD_{sim} at the location where particles assemble (node of the standing ultrasound wave field) as a function of the nondimensional time K_3 for different particle volume fractions $0.5 \leq \Phi \leq 22.5\%$ (Figure 6a), different nondimensional particle sizes $0.05 \leq K_1 \leq 0.20$ (Figure 6b), and different nondimensional fluid medium viscosities $0.07 \leq K_2 \leq 0.27$ (Figure 6c). In addition, Figure 6 shows the nondimensional packing time K_3^* (hollow circles), i.e., the time at which the local particle packing density reaches 90% of its steady-state value. The nondimensional packing time is important, e.g., in the context of VP, where one must know the time required for particles to assemble at their steady-state locations, before curing a layer of photopolymer resin. Consequently, K_3^* also determines the speed of the VP process.

From Figure 6, we observe that the transient local particle packing density PD_{sim} increases and ultimately reaches steady-state with increasing nondimensional time K_3, similar to the results of Figures 4 and 5. Figure 6a shows that increasing particle volume fraction Φ increases the transient local particle packing density prior to reaching its maximum value $PD_{sim} = 45\%$. This result agrees with the maximum achievable steady-state local particle packing density within the pattern features after ultrasound DSA.[51] Additionally, from Figure 6a we observe that

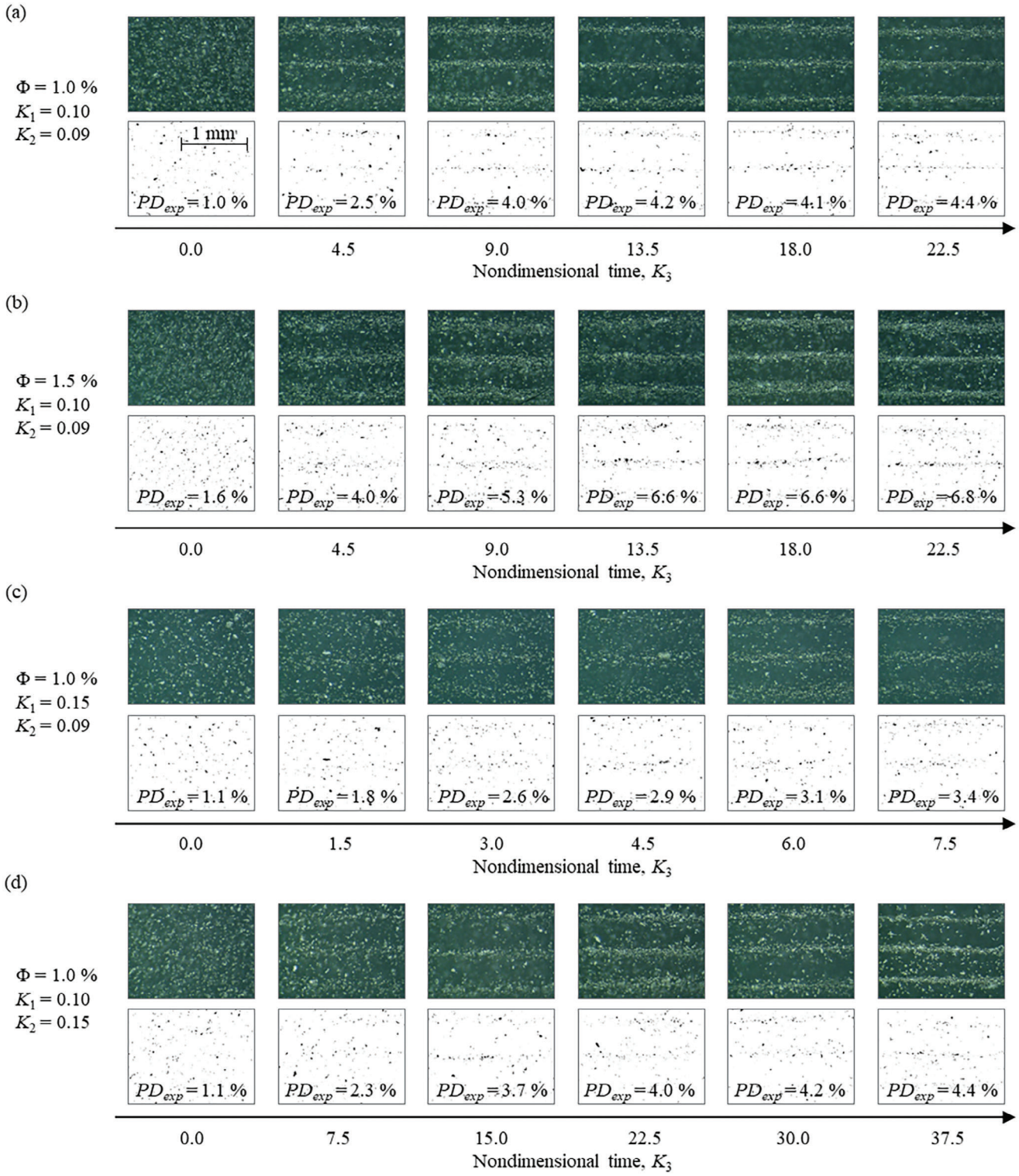

Figure 5. Optical micrographs (green = resin, silver = particles) and binary images (white = resin, black = particles) of composite material specimens for selected data points of Figure 4: a) $\Phi = 1.0\%$, $K_1 = 0.10$, and $K_2 = 0.09$, b) $\Phi = 1.5\%$, $K_1 = 0.10$, and $K_2 = 0.09$, c) $\Phi = 1.0\%$, $K_1 = 0.15$, and $K_2 = 0.09$, and d) $\Phi = 1.0\%$, $K_1 = 0.10$, and $K_2 = 0.15$.

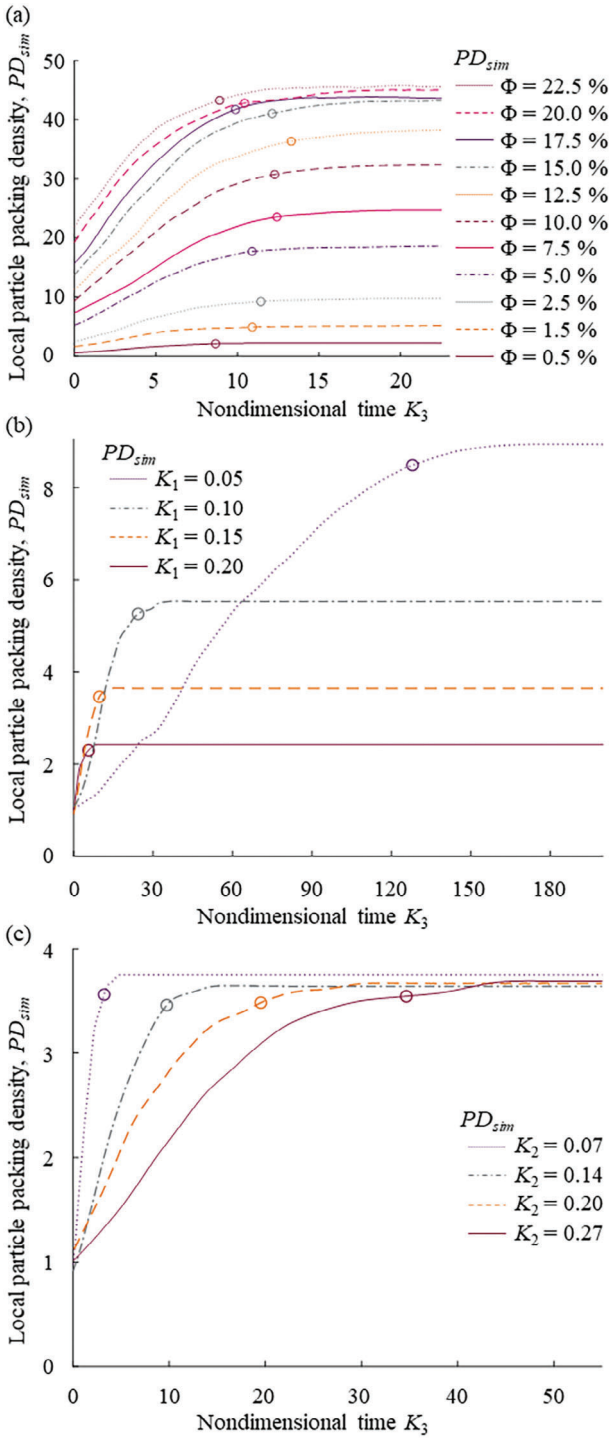

Figure 6. Transient local particle packing density PD_{sim} at locations where particles assemble, as a function of nondimensional time K_3, covering the entire ultrasound DSA process envelope, a) for $K_1 = 0.15$ and $K_2 = 0.14$ and different particle volume fractions $0.5 \leq \Phi \leq 22.5\%$, b) for $\Phi = 1.0\%$ and $K_2 = 0.14$ and different nondimensional particle sizes $0.05 \leq K_1 \leq 0.20$, and c) for $\Phi = 1.0\%$ and $K_1 = 0.15$ and different nondimensional medium viscosities $0.07 \leq K_2 \leq 0.27$, also showing the nondimensional packing time K_3^* (hollow circles) for each transient local particle packing density PD_{sim}.

increasing the particle volume fraction Φ first increases ($\Phi \leq 15\%$) and then decreases ($\Phi > 15\%$) the nondimensional packing time K_3^*, which is the result of two phenomena. First, increasing Φ increases the number of particles in a control volume within the ultrasound DSA reservoir, which increases the number of collisions between particles and also increases the dissipative acoustic interaction forces due to ultrasound wave scattering. Collisions and dissipative acoustic interaction forces decrease the effective particle velocity $||\mathbf{u}||$ with which particles approach the locations where they assemble and, thus, increase K_3^*. However, increasing $\Phi \geq 15\%$ increases the local particle packing density PD_{sim} when particles are initially randomly dispersed at nondimensional time $K_3 = 0$, such that the steady-state PD_{sim} reaches its theoretical maximum value of approximately 45%. Hence, increasing $\Phi \geq 15\%$ decreases the difference between PD_{sim} at $K_3 = 0$ and its steady-state PD_{sim}, which decreases the nondimensional packing time K_3^* because the maximum local particle packing density at the locations where particles assemble is reached before all particles reach their steady-state location. From Figure 6b, we observe that increasing nondimensional particle size K_1 decreases the nondimensional packing time K_3^* because increasing K_1 increases the acoustic radiation force $||\mathbf{F}_a|| \propto a^3$ (Equation 2) more than the drag force $||\mathbf{F}_d|| \propto a$ on particles, which increases the velocity $||\mathbf{u}||$ with which they move toward the locations where they assemble and, consequently, decreases the time to reach that location. Figure 6c shows that increasing the nondimensional fluid medium viscosity K_2 increases the nondimensional packing time K_3^*, but it does not affect the steady-state local particle packing density PD_{sim}, as expected. Increasing K_2 increases the magnitude of drag force on particles $||\mathbf{F}_d|| \propto a$ and, thus, decreases the velocity $||\mathbf{u}||$ with which particles move toward the locations where they assemble, which increases the time to reach that location.

Using the 3D ultrasound DSA model, we quantify the relationship between nondimensional particle size K_1 and nondimensional fluid medium viscosity K_2, and the nondimensional packing time K_3^* and nondimensional packing rate $\delta PD/\delta K_3$, which both characterize the transient local particle packing density PD_{sim}. **Figure 7** shows the nondimensional packing time K_3^* and nondimensional packing rate $\delta PD/\delta K_3$ as a function of nondimensional particle size K_1 for different values of the nondimensional fluid medium viscosity $0.07 \leq K_2 \leq 0.27$. We derive power and linear best-fit equations for K_3^* and $\delta PD/\delta K_3$, respectively, to quantify their relationship with the nondimensional ultrasound DSA process parameters K_1 and K_2. These equations provide information, e.g., to tune the VP layer-by-layer curing process, based on the material properties and ultrasound DSA process parameters. From Figure 7, we observe that increasing nondimensional particle size K_1 decreases the nondimensional packing time K_3^* and increases the nondimensional packing rate $\delta PD/\delta K_3$. Increasing nondimensional particle size K_1 requires increasing the particle radius a, which increases the acoustic radiation force that acts on particles $||\mathbf{F}_a|| \propto a^3$ (see Equation 2), increases the velocity $||\mathbf{u}||$ with which particles move toward the nodes of standing ultrasound wave field, decreases the time particles require to assemble at the node of standing ultrasound wave field and, thus, decrease the nondimensional packing time K_3^*. Also, increasing the velocity $||\mathbf{u}||$ with which

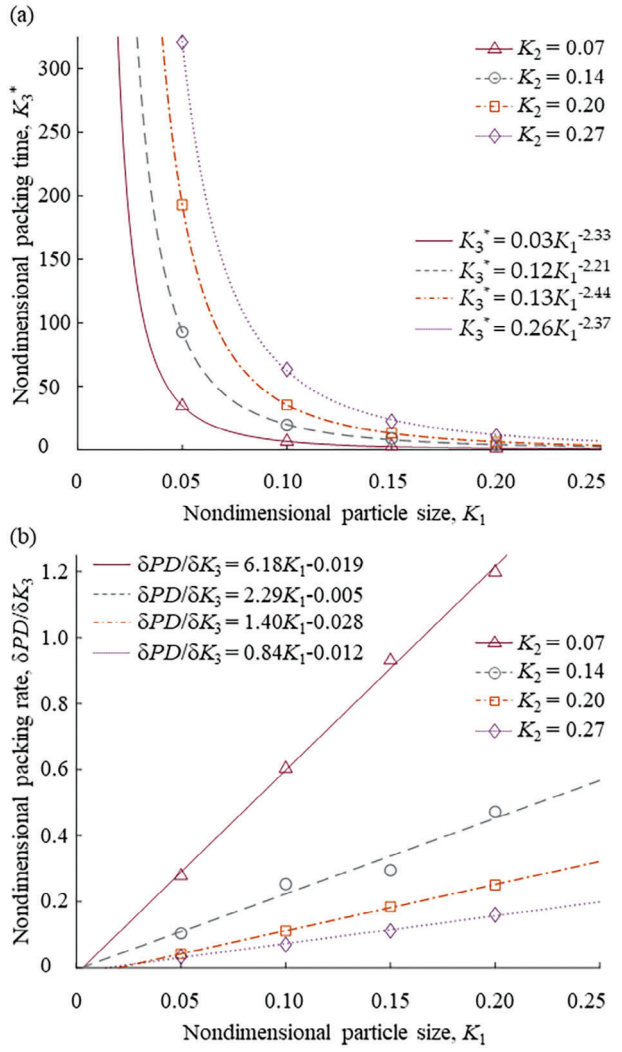

Figure 7. a) Nondimensional packing time K_3^* and b) nondimensional packing rate $\delta PD/\delta K_3$ as a function of nondimensional particle size K_1 for nondimensional fluid medium viscosity $K_2 = 0.07$ (maroon rectangle), $K_2 = 0.14$ (gray circle), $K_2 = 0.20$ (orange square), and $K_2 = 0.27$ (purple diamond), illustrating a) power and b) linear best-fit equations of nondimensional packing time K_3^* and nondimensional packing rate $\delta PD/\delta K_3$ (hollow markers), respectively.

particles move toward the nodes of the standing ultrasound wave field increases the number of particles that assemble at nodes at each time increment during ultrasound DSA and, thus, increases the nondimensional packing rate $\delta PD/\delta K_3$.

Additionally, Figure 7 shows that increasing nondimensional fluid medium viscosity K_2 increases the nondimensional packing time K_3^* and decreases the nondimensional packing rate $\delta PD/\delta K_3$. Increasing K_2 increases the magnitude of the drag force on the particles $||\mathbf{F}_d|| \propto a$ and, thus, decreases the velocity $||\mathbf{u}||$ with which particles move toward the locations where they assemble, which increases the time to reach that location, increases K_3^*, and decreases $\delta PD/\delta K_3$. We note that Figures 6 and 7 include parameter values that extrapolate beyond the range of the experimental validation and, thus, must be interpreted with caution.

3.3. Discussion

The 3D ultrasound DSA model advances existing models through several innovations. First, it is the first model that extends beyond simulating the steady-state locations where particles assemble, which enables quantifying the transient local particle packing density by PD_{sim}, nondimensional packing time K_3^*, and nondimensional packing rate $\delta PD/\delta K_3$ until the particles and the local particle packing density PD_{sim} reach steady-state.[50,51] Second, the model is capable of simultaneously predicting the trajectory of many spherical particles dispersed in a viscous fluid medium during ultrasound DSA, which contrasts existing transient models that theoretically simulate the dynamic behavior of an individual particle in an inviscid medium,[44,49,54–56] and existing studies that only experimentally investigate the dynamic behavior of multiple particles in an inviscid medium.[55,67] However, the results of this work still agree with previous studies that describe the dynamic behavior of an individual particle in a standing ultrasound wave field, which document the effect of particle size a, fluid medium viscosity η_m, and ultrasound frequency f on the transient behavior of the particle.[55] Third, this model relaxes simplifying assumptions of existing models that consider an inviscid medium,[54] and neglects the effects of ultrasound wave attenuation and ultrasound wave scattering from neighboring particles.[55] Finally, this transient model is perhaps the first one to include collisions between particles by means of an LJ-like potential.

The 3D ultrasound DSA model also shows limitations. We define randomly dispersed particles only in a section of the reservoir, i.e., the simulation domain, to manage the computational cost of the simulations. However, this simplification neglects the effect of ultrasound wave scattering by particles outside the simulation domain on the transient local particle packing density PD_{sim}. Thus, the particle packing density at the edges of the simulation domain likely underestimates the true particle packing density. Additionally, one can study the acoustic interaction between spherical particles in a fluid medium using a single or multiple scattering. Single scattering considers only one scattering event, whereas multiple scattering considers multiple scattering events of the scattered wave.[40] The 3D ultrasound DSA model only implements single scattering because, for the range of particle volume fractions we consider in this work, the particles remain far away from each other during the transient portion of the simulation. However, when particles assemble at the nodes of the standing ultrasound wave, using multiple scattering would be more appropriate because a particle is surrounded by many other particles and, thus, the scattered wave can reflect off multiple particles. We did not include multiple scattering due to computational cost, and because the literature predicts its effect to be small.[40]

Quantifying the transient local particle packing density is not straightforward because the locations where particles assemble are not unambiguously defined. The node of a standing wave theoretically is a line, but in practice, particles assemble and agglomerate at a location of finite width, which necessitates defining a rectangular region of width w around the node to quantify the local particle packing density. Consequently, the transient local particle packing density depends on w, i.e., it increases with decreasing w, as an increasing fraction of the domain is occupied by

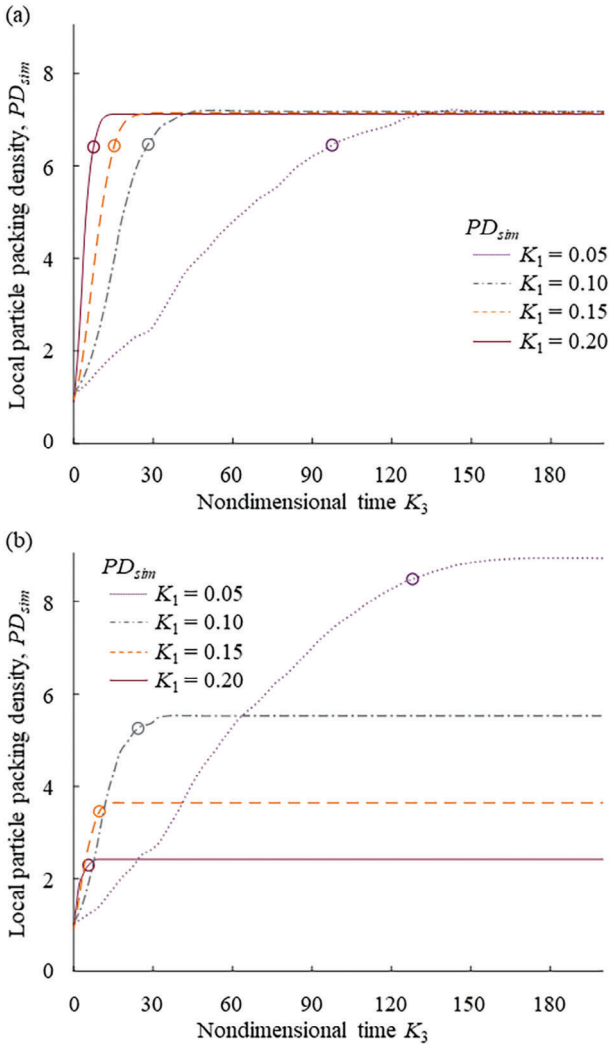

Figure 8. Transient local particle packing density PD_{sim} within the pattern features as a function of nondimensional time K_3, using a a) constant domain of width $w = 60$ µm and (b) a variable domain of width $w = 6a$, covering the entire ultrasound DSA process envelope, for $\Phi = 1.0\%$ and $K_2 = 0.14$ and different nondimensional particle size $0.05 \leq K_1 \leq 0.20$, also illustrating the nondimensional packing time K_3^* (hollow circles) for each transient local particle packing density PD_{sim}.

particles at any given time. We replicate the results of Figure 6b to illustrate the difference between measuring the transient local particle packing density PD_{sim} within a domain width that is a function of the particle radius a, i.e., $w = 6a$, or within a constant domain width w around the node. **Figure 8** shows the transient local particle packing density PD_{sim} at the location where particles assemble as a function of nondimensional time K_3, for a constant domain width $w = 60$ µm (Figure 8a) and for domain width $w = 6a$ (Figure 8b, identical to Figure 6b), for $\Phi = 1.0\%$ and $K_2 = 0.14$ and $0.05 \leq K_1 \leq 0.20$. We also show the nondimensional packing time K_3^* (hollow circles). From Figure 8, we observe that increasing nondimensional particle size K_1 decreases the nondimensional packing time K_3^*, both when $w = 60$ µm and $w = 6a$. However, the magnitude of this reduction is different between both choices of the domain width. Changing K_1 shows no effect on the steady-state local particle packing density PD_{sim} within the domain of constant width w (Figure 8a) since the volume of the domain and the volume of the particles within the domain remain constant. In contrast, increasing K_1 decreases the steady-state local particle packing density PD_{sim} within the variable domain of width $w = 6a$ (Figure 8b) because the width of the domain increases with the size of the particles, thus adding more empty space.

The experiments also show limitations. We validate the 3D ultrasound DSA model over a limited range of ultrasound DSA process parameters, i.e., particle volume fraction $0.50 \leq \Phi \leq 1.50\%$, particle size $a = 15$ and 22 µm, and fluid medium viscosity $\eta_m = 126$ and 218 mPa.s. Thus, the experimental validation does not cover the entire ultrasound DSA process envelope due to practical limitations of increasing Φ, a, and η_m during the experiments (see Section 2.2). In addition, imperfect dispersion of spherical aluminum microparticles in the (diluted) photopolymer resin, imperfect spherical shape and size of the aluminum microparticles, misalignment of the ultrasound transducers on the walls of the acrylic reservoir, and the ultrasound transducers not performing as perfect piston sources, all-cause error in the experimental results.

We note that we chose the amplitude of the ultrasound wave in the experiments based on experimental constraints. Increasing the peak-to-peak voltage $V_{p\text{-}p}$ to the ultrasound transducers increases the amplitude of the standing ultrasound wave and, consequently, increases the acoustic radiation force that acts on particles in the reservoir. Thus, increasing $V_{p\text{-}p}$ increases the velocity with which particles move to the nodes of the standing ultrasound wave. However, increasing $V_{p\text{-}p}$ also increases the temperature of the medium, and increases the likelihood of acoustic streaming that distorts the assembly of particles into patterns. Hence, we balance both effects by selecting $V_{p\text{-}p}$ sufficiently high to organize particles at the nodes of the standing ultrasound wave before they precipitate to the bottom of the reservoir, yet sufficiently low to avoid heating and acoustic steaming that distort the assembly of particles into specific patterns.

Finally, we emphasize that even though we manufacture single-layer specimens in this work, we have previously demonstrated that the integration of ultrasound DSA and VP can implement multilayer specimens, by following a two-step curing approach that allows establishing an ultrasound in the photopolymer resin contained in the VP vat.[23]

4. Conclusion

This work presents a 3D model of ultrasound DSA that enables simulating the trajectories of many spherical particles dispersed in a viscous fluid medium, subject to a standing ultrasound wave field, as a function of time and ultrasound DSA process parameters. Such simulations allow quantifying the transient and steady-state local particle packing density at the specific locations where the particles assemble. We demonstrate good agreement between the theoretical model and experiments. We conclude that:

1. The local particle packing density at locations where particles assemble increases with increasing nondimensional time K_3 due to the increasing number of particles that assemble at a specific location, then reaches steady-state when almost all

particles have assembled at a specific location. Furthermore, the local particle packing density increases with increasing particle volume fraction Φ due to an increasing number of particles dispersed in the photopolymer. It ultimately reaches a steady-state particle packing density that approaches the theoretical random particle packing density for spherical particles of approximately 45%.

2. Increasing the nondimensional particle size K_1 decreases the local particle packing density for constant particle volume fraction Φ because the number of particles to obtain a specific Φ decreases with increasing K_1. In addition, increasing the nondimensional fluid medium viscosity K_2 decreases the transient local particle packing density for constant particle volume fraction Φ because increasing the fluid medium viscosity increases the drag force on the particles $||\mathbf{F}_d||$ and decreases the velocity $||\mathbf{u}||$ with which they approach their steady-state location. However, the steady-state local particle packing density remains unaffected by the nondimensional fluid medium viscosity K_2.
3. Increasing the particle volume fraction Φ first increases and then decreases the nondimensional packing time K_3^* because increasing Φ increases collisions and ultrasound wave scattering between particles that decrease the velocity $||\mathbf{u}||$ with which particles move toward locations where they assemble. Increasing $\Phi \geq 15\%$ increases the local particle packing density when particles are initially randomly dispersed in the fluid medium, such that the steady-state local particle packing density reaches its theoretical maximum value of approximately 45%. Hence, K_3^* decreases because the local particle packing density at the locations where particles assemble reaches its maximum value before all particles reach their steady-state location. Increasing the nondimensional particle size K_1 or decreasing nondimensional fluid medium viscosity K_2 both increase the velocity with

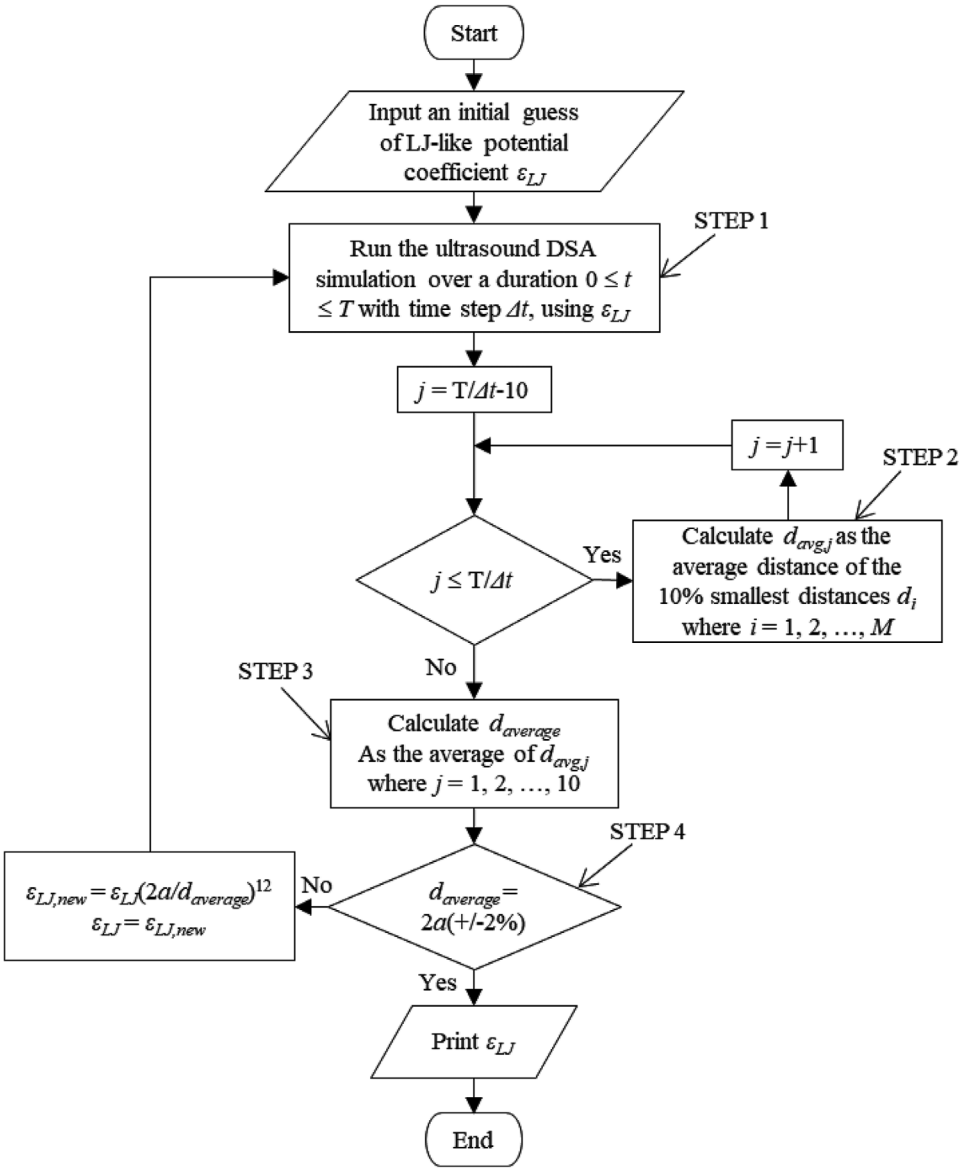

Figure A1. Flowchart of the ϵ_{LJ} parameter tuning procedure.

which particles move toward the locations where they assemble and, thus, decrease K_3^*.

The results of this work provide a physical understanding of the transient phenomena that affect the local particle packing density during ultrasound DSA in a viscous fluid medium. This knowledge is relevant to a broad spectrum of engineering applications that involve ultrasound DSA, such as noncontact particle manipulation, lab-on-a-chip applications, acoustic displays, and materials manufacturing. Specifically, with respect to integrating ultrasound DSA and VP to manufacture engineered composite materials, the results of this work allow tailoring the layer-by-layer VP process to the ultrasound DSA process parameters and manufacture composite materials wherein each layer, ultrasound DSA organizes and orients particles into specific patterns with specific local particle packing density before the VP process cures a new layer.

5. Appendix: Iterative tuning procedure of ϵ_{LJ} parameter

We consider both particle–particle and particle–wall interactions in the ultrasound DSA simulations, using the LJ-like potentials $V_{\mathrm{LJ,p\text{-}p}} = 4\epsilon_{LJ}(2a/r_{\mathrm{p\text{-}p}})^{12}$ and $V_{\mathrm{LJ,p\text{-}w}} = 4\epsilon_{LJ}(a/r_{\mathrm{p\text{-}w}})^{12}$, respectively. The parameter ϵ_{LJ} is the same for particle–particle and particle–wall interactions. $r_{\mathrm{p\text{-}p}}$ is the distance between a pair of particles, and $r_{\mathrm{p\text{-}w}}$ is the distance between a particle and a simulation domain boundary. Hence, tuning of the LJ-like potential ensures a minimum separation of $2a$ and a between particle–particle and particle–wall, respectively, where a is the radius of a particle. To determine the ϵ_{LJ} parameter, we perform the following tuning process (see flowchart of **Figure A1**):

STEP 1: We perform the ultrasound DSA simulation over a duration $0 \leq t \leq T$ with time step Δt and an initial guess of ϵ_{LJ}, which is based on experience and values that have previously worked. However, we note that the methodology works for any initial guess; it could just require more iterations to reach a converged solution based on the choice of the initial guess. We choose T long enough so the particles assemble at the nodes of the standing ultrasound wave and reach a steady-state local packing density.

STEP 2: After particles assemble at nodes of the standing ultrasound wave, we measure the distance between each particle and its closest neighboring particle d_i where $i = 1, 2, \ldots, M$ (M is the number of particles assembled in a domain $w = 6a$ centered around a node of the standing ultrasound wave.). We calculate the average distance d_{avg} of the 10% smallest distances d_i.

STEP 3: We repeat STEP 2 for the ten sequential time steps before $t = T$, when the particles have already assembled at the node of the standing ultrasound wave, and the particle packing density remains unchanged. We calculate $d_{\mathrm{avg,j}}$ for each time step, with $j = 1, 2, \ldots, 10$. Then, we calculate the average of all $d_{\mathrm{avg,j}}$ values as d_{average}. Hence, in steps 2 and 3, we average the minimum distance between particles over both space (STEP 2) and time (STEP 3).

STEP 4: We use an automated iterative optimization method by repeating STEPs 1–3, until $d_{\mathrm{average}} = 2a$ (+/−2%). Therefore, we tune $\epsilon_{\mathrm{LJ,new}} = \epsilon_{LJ}(2a/d_{\mathrm{average}})^{12}$ in each iteration so particles experience a magnitude of $V_{\mathrm{LJ,p\text{-}p}}$ at $r_{\mathrm{p\text{-}p}} = 2a$ that equals the magnitude of $V_{\mathrm{LJ,p\text{-}p}}$ at $r_{\mathrm{p\text{-}p}} = d_{\mathrm{average}}$ in the previous iteration. Thus, if $d_{\mathrm{average}} > 2a$, we increase the "spring constant" of the LJ-like potential to draw the particles closer, and if $d_{\mathrm{average}} < 2a$, we decrease the "spring constant" of the LJ-like potential so that the equilibrium distance between particles increases. We repeat the described iterative optimization method for all simulations in this work.

Acknowledgements

S.N., M.F., and B.R. acknowledge the support of the National Science Foundation under award CMMI-2130083. FGV acknowledges the support of the National Science Foundation under awards DMS-2008610 and DMS-2136198.

Conflict of Interest

The authors declare no conflict of interest.

Data Availability Statement

The data that support the findings of this study are available from the corresponding author upon reasonable request.

Keywords

transient, ultrasound directed self-assembly, vat photopolymerization, viscosity

Received: November 14, 2023
Revised: March 15, 2024
Published online:

[1] J. Greenhall, F. G. Vasquez, B. Raeymaekers, *Appl. Phys. Lett.* **2016**, *108*, 103103.
[2] M. Prisbrey, B. Raeymaekers, *Phys. Rev. Applied* **2019**, *12*, 014014.
[3] S. Mohanty, I. S. M. Khalil, S. Misra, *Proc. R. Soc. A* **2020**, *476*, 20200621.
[4] A. Marzo, S. A. Seah, B. W. Drinkwater, D. R. Sahoo, B. Long, S. Subramanian, *Nat. Commun.* **2015**, *6*, 8661.
[5] A. G. Guex, N. Di Marzio, D. Eglin, M. Alini, T. Serra, *Mater. Today Bio.* **2021**, *10*, 100110.
[6] R. Hirayama, D. Martinez Plasencia, N. Masuda, S. Subramanian, *Nature* **2019**, *575*, 320.
[7] T. Fushimi, A. Marzo, B. W. Drinkwater, T. L. Hill, *Appl. Phys. Lett.* **2019**, *115*, 064101.
[8] Y. Ochiai, T. Hoshi, J. Rekimoto, *ACM Trans. Graph.* **2014**, *33*, 1.
[9] L. Tian, N. Martin, P. G. Bassindale, A. J. Patil, M. Li, A. Barnes, B. W. Drinkwater, S. Mann, *Nat. Commun.* **2016**, *7*, 13068.
[10] C. IV Wyatt Shields, C. D. Reyes, G. P. López, *Lab Chip* **2015**, *15*, 1230.
[11] S. Kawasaki, J.-J. Yeh, M. Saccher, J. Li, R. Dekker, in *2022 IEEE 35th International Conference on Micro Electro Mechanical Systems Conference (MEMS)*, IEEE, Tokyo, Japan, **2022**, pp. 908–911.
[12] P. Juliano, M. A. Augustin, X.-Q. Xu, R. Mawson, K. Knoerzer, *Ultrason. Sonochem.* **2017**, *35*, 577.
[13] S. Mettu, S. Yao, Q. Sun, S. R. Lawson, P. J. Scales, G. J. O. Martin, M. Ashokkumar, *Ind. Eng. Chem. Res.* **2020**, *59*, 7901.

[14] Y. Zhang, X. Chen, *Ultrason. Sonochem.* **2021**, *75*, 105603.
[15] E. V. Skorb, H. Möhwald, T. Irrgang, A. Fery, D. V. Andreeva, *Chem. Commun.* **2010**, *46*, 7897.
[16] M. D. Haslam, B. Raeymaekers, *Compos. B: Eng.* **2014**, *60*, 91.
[17] J. Greenhall, L. Homel, B. Raeymaekers, *J. Compos. Mater.* **2019**, *53*, 1329.
[18] T. A. Ogden, M. Prisbrey, I. Nelson, B. Raeymaekers, S. E. Naleway, *Mater. Des.* **2019**, *164*, 107561.
[19] M. Mroz, J. L. Rosenberg, C. Acevedo, J. J. Kruzic, B. Raeymaekers, S. E. Naleway, *Materialia* **2020**, *12*, 100754.
[20] R. R. Collino, T. R. Ray, R. C. Fleming, C. H. Sasaki, H. Haj-Hariri, M. R. Begley, *Extreme Mech. Lett.* **2015**, *5*, 37.
[21] P. Wadsworth, I. Nelson, D. L. Porter, B. Raeymaekers, S. E. Naleway, *Mater. Des.* **2020**, *185*, 108243.
[22] L. Friedrich, R. Collino, T. Ray, M. Begley, *Sens. Actuators A: Phys.* **2017**, *268*, 213.
[23] J. Greenhall, B. Raeymaekers, *Adv. Mater. Technol.* **2017**, *2*, 1700122.
[24] D. E. Yunus, S. Sohrabi, R. He, W. Shi, Y. Liu, *J. Micromech. Microeng.* **2017**, *27*, 045016.
[25] T. M. Llewellyn-Jones, B. W. Drinkwater, R. S. Trask, *Smart Mater. Struct.* **2016**, *25*, 02LT01.
[26] K. Niendorf, B. Raeymaekers, *Compos. Part A Appl. Sci. Manuf.* **2020**, *129*, 105713.
[27] L. Lu, Z. Zhang, J. Xu, Y. Pan, *Compos. B: Eng.* **2019**, *174*, 106991.
[28] L. P. Gor'kov, *Sov. Phys.-Dokl.* **1962**, *6*, 773.
[29] X. Chen, R. E. Apfel, *J. Acoust. Soc. Am.* **1996**, *99*, 713.
[30] M. Settnes, H. Bruus, *Phys. Rev. E* **2012**, *85*, 016327.
[31] L. V. King, *Phys. R. Soc. London A Mat.* **1934**, *147*, 212.
[32] K. Yosioka, Y. Kawasima, *Acustica* **1955**, *5*, 167.
[33] J. Wu, G. Du, *J. Acoust. Soc. Am.* **1990**, *87*, 997.
[34] W. König, *Ann. Phys. (Leipzig)* **1891**, *278*, 549.
[35] V. F. K. Bjerknes, *Fields of Force: A Course of Lectures in Mathematical Physics Delivered December 1 to 23, 1905*, Columbia University Press, New York, **1906**.
[36] T. F. W. Embleton, *J. Acoust. Soc. Am.* **1962**, *34*, 1714.
[37] W. L. Nyborg, *Ultrasound Med. Biol.* **1989**, *15*, 93.
[38] A. P. Zhuk, *Sov. Appl. Mech.* **1985**, *21*, 307.
[39] S. Sepehrirahnama, F. S. Chau, K.-M. Lim, *Phys. Rev. E* **2016**, *93*, 023307.
[40] G. T. Silva, H. Bruus, *Phys. Rev. E* **2014**, *90*, 063007.
[41] M. Barmatz, P. Collas, *J. Acoust. Soc. Am.* **1985**, *77*, 928.
[42] Y. Ochiai, T. Hoshi, J. Rekimoto, *PLoS One* **2014**, *9*, e97590.
[43] M. Prisbrey, J. Greenhall, F. G. Vasquez, B. Raeymaekers, *J. Appl. Phys.* **2017**, *121*, 014302.
[44] C. R. P. Courtney, C.-K. Ong, B. W. Drinkwater, A. L. Bernassau, P. D. Wilcox, D. R. S. Cumming, *Proc. Math. Phys. Eng. Sci.* **2011**, *468*, 337.
[45] A. L. Bernassau, C. R. P. Courtney, J. Beeley, B. W. Drinkwater, D. R. S. Cumming, *Appl. Phys. Lett.* **2013**, *102*, 164101.
[46] M. Prisbrey, B. Raeymaekers, *Phys. Rev. Appl.* **2018**, *10*, 034066.
[47] M. Prisbrey, F. G. Vasquez, B. Raeymaekers, *Appl. Phys. Lett.* **2020**, *117*, 111904.
[48] M. Prisbrey, F. G. Vasquez, B. Raeymaekers, *Phys. Rev. Appl.* **2020**, *14*, 024026.
[49] J. Greenhall, F. G. Vasquez, B. Raeymaekers, *Appl. Phys. Lett.* **2014**, *105*, 144105.
[50] S. Noparast, F. G. Vasquez, B. Raeymaekers, *J. Appl. Phys.* **2022**, *131*, 134901.
[51] S. Noparast, F. G. Vasquez, M. Francoeur, B. Raeymaekers, *Phys. Rev. Appl.* **2023**, *19*, 064087.
[52] J.-H. Xie, J. Vanneste, *Phys. Fluids* **2014**, *26*, 102001.
[53] A. N. Guz, A. P. Zhuk, *Int. Appl. Mech.* **2004**, *40*, 246.
[54] A. Haake, J. Dual, *J. Acoust. Soc. Am.* **2005**, *117*, 2752.
[55] M.-S. Scholz, B. W. Drinkwater, T. M. Llewellyn-Jones, R. S. Trask, *IEEE Trans. Ultrason. Ferroelectr. Freq. Control* **2015**, *62*, 1845.
[56] N. Aboobaker, D. Blackmore, J. Meegoda, *Appl. Math. Model.* **2005**, *29*, 515.
[57] R. Weser, Z. Deng, V. V. Kondalkar, A. N. Darinskii, C. Cierpka, H. Schmidt, J. König, *Lab Chip* **2022**, *22*, 2886.
[58] A. R. Khan, J. F. Richardson, *Chem. Eng. Commun.* **1987**, *62*, 135.
[59] X. Wang, S. Ramírez-Hinestrosa, J. Dobnikar, D. Frenkel, *Phys. Chem. Chem. Phys.* **2020**, *22*, 10624.
[60] K. Uchino, *Advanced Piezoelectric Materials: Science and Technology*, Woodhead Publishing, Sawston, Cambridge **2017**.
[61] L. E. Kinsler, L. E. Kinsler, A. R. Frey, A. B. Coppens, J. V. Sanders, *Fundamentals of Acoustics*, Wiley, Hoboken, NJ **2000**.
[62] J. Liang, M. Francoeur, C. B. Williams, B. Raeymaekers, *ACS Appl. Polym. Mater.* **2023**, *5*, 9017.
[63] W. M. Haynes, D. R. Lide, T. J. Bruno, *CRC Handbook of Chemistry and Physics*, CRC Press, Boca Raton, **2014**.
[64] E. R. Weibel, *Morphometry of the Human Lung*, Springer, Berlin, Heidelberg **1963**.
[65] E. E. Underwood, *J. Microsc.* **1969**, *89*, 161.
[66] E. R. Weibel, D. M. Gomez, *J. Appl. Physiol.* **1962**, *17*, 343.
[67] A. Franklin, A. Marzo, R. Malkin, B. W. Drinkwater, *Appl. Phys. Lett.* **2017**, *111*, 094101.